Journal of Sensor Science and Technology
Vol. 33, No. 5 (2024) pp. 288-297
http://dx.doi.org/10.46670/JSST.2024.33.5.288
pISSN 1225-5475/eISSN 2093-7563

# Synthesis and Oxidation Behavior of Pd-Ir@$CeO_2$ Core-shell Nanoparticles for Hydrogen Gas Sensor

**Gi-Seung Shin[1,*], Dong-Seog Kim[1,*], Tuong Van Tran[1], Geun-Jae Oh[1], Seok-Yong Hong[2], Ho-Geun Song[3], and Yeon-Tae Yu[1,+]**

## Abstract

Currently, numerous studies are being conducted on metal oxide semiconductor (MOS) gas sensors for hydrogen detection, using Palladium (Pd) and Pd-based alloy nanoparticles (NPs) owing to their hydrogen absorption ability. Furthermore, several studies have reported that Pd-Iridium (Ir) alloys possess high hydrogen absorption capabilities in their bulk state. However, Ir growth is limited to above 2 nm and it does not mix extensively with other metals. Furthermore, as the hydrogen absorption capacity decreases with the reduction in particle size, it is necessary to synthesize nanoparticles of an appropriate size. Therefore, the synthesis of Pd-Ir alloy NPs larger than 10 nm is challenging. In this study, we report the synthesis of Pd-Ir NPs with an average diameter of 19 nm using a hydrothermal technique for the first time and fabricated Pd-Ir alloy NPs through calcination at 500°C in Ar and air. To confirm alloy formation and oxidation behavior, X-ray diffraction (XRD) and X-ray photoelectron spectroscopy (XPS) were performed. In addition, we synthesized Pd-Ir@$CeO_2$ core-shell nanoparticles (CSNPs) as hydrogen gas-sensing materials. The Pd-Ir core was partially oxidized during heat treatment at 500°C in air, and Pd-Ir@$CeO_2$ CSNPs were finally changed into Pd-Ir(alloy)/PdO-$IrO_2$@$CeO_2$ CSNPs, which exhibited higher sensitivity and selectivity toward $H_2$ gas compared to totally oxidized PdO-$IrO_2$@$CeO_2$ CSNPs and pure $CeO_2$ NPs. The enhanced gas-sensing performance was attributed to the hydrogen absorption effect of the Pd-Ir(alloy) NPs.

**Keywords:** Metal oxide semiconductor, Pd-Ir alloy, Core-shell, Nanoparticle, Gas sensor, Hydrogen

## 1. INTRODUCTION

The global trend of transitioning from fossil fuels to renewable and clean energy sources stems from concerns about environmental pollution and resource depletion. Among the promising alternative energy sources, hydrogen stands out because of its environmental friendliness, high energy density, and inexhaustibility [1-3]. Nonetheless, hydrogen is a colorless, odorless, and leak-prone gas with a wide explosive concentration range, making it important to develop reliable and inexpensive gas detection systems [4-6].

Metal-oxide semiconductor (MOS) gas sensors have attracted significant attention for gas detection [7-9]. These materials are favored because of their high stability, simple operating principles, and responses to most gases. In particular, $CeO_2$ has emerged as a leading gas sensing material owing to its 4f electron shell, low redox potential between $Ce^{3+}$ and $Ce^{4+}$ states, and high density of oxygen vacancies [10-12]. For example, Hussain et al. synthesized polyhedral $CeO_2$ nanoparticles (NPs) by hydrothermal method, which exhibited high sensitivity and selectivity to 150 ppm HCHO at 220°C [13]. Dao et al. fabricated $CeO_2$ NPs by the ionic liquid-supported method, which showed a high response to 100 ppm ethanol at 400°C [14]. Despite their potential, MOS gas sensors face challenges such as high operating temperatures, low sensitivity, and poor selectivity for hydrogen gas [15-17]. To address these issues, researchers have integrated noble metal catalysts into MOS sensors to enhance their gas-sensing properties through catalytic effects containing chemical and electronic sensitization [18-20].

Palladium (Pd) has been widely studied as a catalyst for hydrogen gas sensing because of its unique ability to absorb hydrogen gas and form metal hydrides, thereby changing the electric charge distribution via chemical reactions on the surface

[1] Division of Advanced Materials Engineering, Research Center for Advanced Materials Development, Jeonbuk National University Jeonju 54896, Republic of Korea
[2] ALLIX, Inc., Jeonju 54853, Republic of Korea
[3] Ogam technology Co., Jinwon, Jangseong 57247, Republic of Korea
*These authors have contributed equally to this work and should be considered co-first authors
+Corresponding author: yeontae@jbnu.ac.kr
(Received : Aug. 20, 2024, Revised : Sep. 2, 2024, Accepted : Sep. 16, 2024)

[21-24]. For instance, Cai et al. reported Pd/$Fe_2O_3$-NiO nanofibers prepared by the electrospinning method, which exhibited high hydrogen selectivity against $NO_2$, ethanol, CO, toluene, $H_2S$, and acetone gases at 250°C [25]. Meng et al. reported that Pd/$SnO_2$ nanoparticles, synthesized via hydrothermal and chemical reduction methods, exhibited a high response toward 500 ppm $H_2$ at a low temperature of 125°C [26]. Thathsara et al. decorated Pd nanoparticles on hollow $TiO_2$ nanospheres via a chemical reduction method using $SiO_2$ nanospheres as a template, which exhibited high sensitivity and selectivity in a wide concentration range from 50 to 10,000 ppm $H_2$ with irradiation of UV light at 80°C [27].

However, the Pd-based MOS gas sensor has the drawback that the Pd catalyst NPs are easily oxidized to PdO at an operating temperature above 200°C. Hence, they are not yet suitable for industrial applications [28-31]. To address these issues, researchers have explored the use of Pd-based alloys as catalysts. For instance, Pandey et al. reported that the Pd-Ag@SnO/$SnO_2$ nanosheet synthesized by hydrothermal and chemical reduction methods showed a high response toward 100 ppm $H_2$ at 225°C and high selectivity toward hydrogen over ethanol, $NH_3$, $NO_2$, CO, and $CO_2$ gases [32]. Choi et al. discovered that Au-Pd/$SnO_2$ nanosheets showed a high sensor signal response to hydrogen and high selectivity of hydrogen toward $CH_4$ gas [33]. Li et al. reported that PdPt@$In_2O_3$ nanocomposites demonstrated a significant detection performance for 100 ppm $H_2$ at room temperature with high selectivity for ammonia, benzene, acetone, ethanol, formaldehyde, and ether gases [34]. Among Pd-based alloys, Pd–iridium (Ir) alloys have been reported to exhibit superior hydrogen absorption performance [35-37]. Nevertheless, because Ir is resistant to growth beyond 2 nm, controlling its size and shape at the nanoscale poses significant challenges [38,39]. However, the hydrogen absorption capacity diminishes with decreasing particle size at the nanoscale [40,41], limiting the use of Pd-Ir alloy NPs as catalysts for hydrogen gas detection. Furthermore, Ir is broadly immiscible with most other metals in the periodic table [42]. Consequently, there have been no reports on the synthesis of Pd-Ir alloy NPs with diameters larger than 10 nm.

In this study, we report, for the first time, a hydrothermal method for preparing Pd–Ir alloy NPs with an average size of 19 nm. The Pd–Ir NPs were coated with $CeO_2$, which protects them from oxidation and agglomeration and serves as the main site for gas reaction, to fabricate Pd–Ir@$CeO_2$ core-shell nanoparticles (CSNPs), and the oxidation behaviors of the Pd–Ir alloy cores during the heat treatment at 500°C were investigated. The degree of oxidation of the Pd-Ir alloy cores is an important factor for hydrogen gas sensing. The hydrogen gas response and selectivity of the Pd–Ir(alloy)/PdO-$IrO_2$@$CeO_2$ CSNPs after heat treatment were investigated in detail, and a reaction mechanism was proposed based on these results.

## 2. EXPERIMENTAL

### 2.1 Materials

Palladium chloride (Sigma Aldrich, 99%), iridium chloride trihydrate (Thermo Scientific, 53-56% Ir), cerium nitrate hexahydrate (Sigma Aldrich, 99%), anhydrous sodium carbonate (Oriental Chemical Industries, 99%), polyvinylpyrrolidone (Sigma Aldrich, PVP; Mw: ~55,000), potassium bromide (Alfa Aesar, 99%), ultrapure water (Millipore, 18.2 MΩ·cm) were used as precursor materials without further treatment. Sodium tetrachloropalladate ($Na_2PdCl_4$) solution was prepared by dissolving 1.0 g of palladium chloride ($PdCl_2$) and 0.66 g of sodium chloride (NaCl) in 100 mL of $H_2O$ at room temperature, with continuous stirring overnight.

### 2.2 Synthesis of Pd-Ir nanoparticles

For the synthesis of Pd-Ir NPs using the hydrothermal method, an aqueous solution was first prepared by mixing 100 mg of PVP, 720 mg of KBr, and 13.746 mL of DI water in a 100 mL glass vessel. Subsequently, 0.804 mL of the prepared $Na_2PdCl_4$ (0.056 M) precursor and 0.45 mL of the $IrCl_3$ (0.1 M) precursor were added and stirred for 10 min. This solution was transferred to a 100 mL Teflon-lined autoclave, which was then heated to 180°C for 4 hours and subsequently cooled to room temperature. Upon completion of the reaction, the Pd-Ir NPs colloid was centrifuged at 15,000 rpm for 30 min to remove the by-products.

### 2.3 Synthesis of Pd-Ir@$CeO_2$ core-shell nanoparticles

A schematic of the synthesis procedure for the Pd-Ir@$CeO_2$ CSNPs is shown in Fig. 1(a). The prepared Pd-Ir NPs were dispersed in 90 mL of deionized (DI) water. A mixture containing 60 mL of the Pd-Ir alloy NPs colloid, 6 mL of $Na_2CO_3$ (50 mM), and 4.8 mL of $Ce(NO_3)_3$ (50 mM) was stirred for 10 min. Subsequently, the mixture was refluxed at 90°C for 12 hours to synthesize Pd-Ir@$CeO_2$ CSNPs. The samples were washed several times with water and ethanol, and then dried. Afterward, Pd-Ir@$CeO_2$ CSNPs were calcinated at 500°C in Ar and air

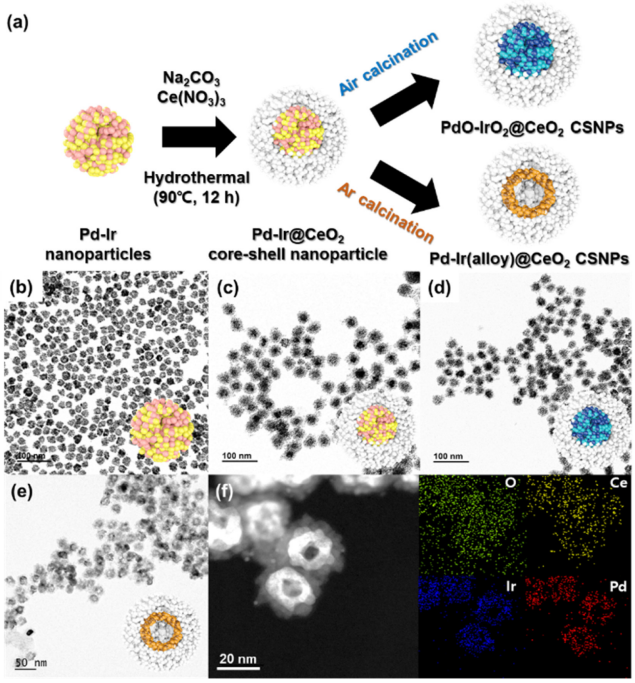


**Fig. 1.** (a) Schematic illustration for the formation procedure of Pd-Ir(alloy)@$CeO_2$ CSNPs and PdO-$IrO_2$@$CeO_2$ CSNPs; TEM images of (b) Pd-Ir NPs, (c) Pd-Ir@$CeO_2$ CSNPs, (d) PdO-$IrO_2$@$CeO_2$ CSNPs, and (e) Pd-Ir(alloy)@$CeO_2$ CSNPs; (f) HAADF image and the corresponding EDS mapping of Pd-Ir(alloy)@$CeO_2$ CSNPs.

atmosphere to investigate the alloy formation and oxidation behavior of Pd-Ir NPs. The samples calcinated in air and Ar are denoted $PdIrO_x$@$CeO_2$ CSNPs and Pd-Ir(alloy)@$CeO_2$ CSNPs, respectively. Additionally, the sample calcinated in Ar was further calcinated in air, and the core was partially oxidized during this process; thus, it was named Pd-Ir(alloy)/PdO-$IrO_2$@$CeO_2$ CSNPs.

### 2.4 Characterization

The sample morphology was analyzed using transmission electron microscopy (TEM, JEOL, JEM-2010) at an accelerating voltage of 100 kV and high-resolution transmission electron microscopy (HRTEM) with Cs-corrected STEM/TEM (JEOL, JEM-2100F) at an accelerating voltage of 200 kV. For TEM analysis, the materials were dropped onto a form bar/carbon-supported copper grid and dried at 60°C overnight. The crystal structure of materials was measured using X-ray diffractometry (D8 Advance, Bruker) with CuKα radiation (λ = 1.54178 Å) at an X-ray power of 40 kV and 40 mA. The chemical bonding states were analyzed by X-ray photoelectron spectroscopy (XPS: Nexsa XPS system, Thermo Fisher Scientific, UK) by using monochromated Al Kα X-ray photon (hv = 1,486.6 eV) sources. To analyze the XPS spectra, the binding energies of the adventitious carbon (C 1s) peak observed at approximately 284.8 eV were used to calibrate the other peaks. The chemical compositions of the samples were analyzed using inductively coupled plasma microscopy (ICPS-7500, Shimadzu Co.).

### 2.5 Gas sensing device fabrication and measurement

To fabricate the sensor devices, gold wires were attached to Pt interdigitated electrodes on an alumina circuit board (Ogam Technology Co. Ltd, electrode part size = 10 mm × 10 mm) using gold paste, and then sintered at 500°C for 2 hours with a heating rate of 1°C/min to remove organics. Next, the circuit board was taped on four sides using sellotape. Subsequently, 0.04 g of the as-prepared powder was uniformly mixed with one drop of α-terpineol. This mixture was thoroughly blended in a mortar to form a paste, which was then applied to a circuit board with platinum electrodes to create a film. After the device dried at 60°C overnight, the tape was removed. The devices were then annealed at 500°C for 2 h at a rate of 1°C/min in a muffle furnace to remove the solvent.

The gas sensing characteristics of the fabricated devices were tested within a temperature range of 200-400°C and a concentration range of 2-100 ppm. A gas-sensing test system was designed to simulate the environmental conditions for evaluating the sensor devices. Each sensor was assessed individually in a highly dynamic chamber that mixed the target gas, $N_2$ (background gas), and dry air (21% oxygen). The gas flow rate within the mass flow controller (MFC) was continuously maintained at 100 sccm through computer management. During the sensing process, air and $N_2$ were mixed to achieve 10.5% oxygen. While the gas sensing test was conducted, the resistance change was recorded using a high resistance meter (Agilent 34970A). The gas sensing response ($R_s$) was defined as $(R_a-R_g)/R_g \times 100$ (%), where $R_a$ and $R_g$ represent the saturated sensor resistance in 10.5% oxygen and after injection of the target gas, respectively.

## 3. RESULTS AND DISCUSSIONS

### 3.1 Material characterizations

The morphologies and sizes of the synthesized nanoparticles were examined using TEM. As shown in Fig. 1(b), the TEM image reveals that the as-synthesized Pd-Ir NPs are aggregates of primary particles with an average diameter of 4.5 nm, and the

average diameter of these aggregates is 19 nm. Fig. 1(c) presents a TEM image of the as-synthesized Pd-Ir@$CeO_2$ CSNPs, which exhibit a core-shell structure with sizes ranging from 36 nm to 42 nm. Fig. 1(d) shows the TEM image of PdO-$IrO_2$@$CeO_2$ CSNPs formed after air calcination at 500°C, confirming that the size of these nanoparticles decreased to 28-37 nm (from 36-42 nm of Pd-Ir@$CeO_2$) as a result of thermal shrinkage and the removal of organic groups. Fig. 1(e) illustrates the TEM image of Pd-Ir(alloy)@$CeO_2$ CSNPs formed after Ar calcination at 500°C, demonstrating that core morphology changed into a hollow structure. The shape transformation can be attributed to the Kirkendall effect, which occurs because of the difference in diffusion rates between the Pd and Ir atoms [43]. In addition, the size of these nanoparticles decreased to 27-32 nm. To analyze the nanostructure of the core-shell nanoparticles in more detail, high-angle annular dark-field (HAADF) and mapping analyses using energy-dispersive X-ray spectroscopy (EDS) were performed as shown in Fig. 1(f), where the presence of O, Ce, Ir, and Pd elements is highlighted in green, yellow, blue, and red, respectively. The results indicate that Pd and Ir elements were concentrated in the core, whereas Ce and O were distributed around the core.

The crystallographic properties and oxidation behavior of the synthesized materials were investigated by X-ray diffraction (XRD). Fig. 2(a) shows the XRD profiles of three samples of Pd-Ir NPs heat-treated at 500°C in different atmospheres: 1) in Ar atmosphere for 2 h, 2) in air atmosphere for 2 h, and 3) in Ar atmosphere for 2 h followed by an additional heat treatment in air. The peaks at 40.9°, 45.8°, and 69° correspond to the (111), (200), and (220) planes of the standard X-ray diffraction pattern of fcc-Ir (JCPDS-06-0598), and the peaks at 40.1°, 46.6°, 68.1°, and 82.1° correspond to the (111), (200), (220), and (311) planes of the standard X-ray diffraction pattern of fcc-Pd (JCPDS-46-1043). The XRD profiles of the as-synthesized Pd-Ir NPs were compared with the individual patterns of Pd and Ir. The peak position of the (111) plane in the as-synthesized Pd-Ir NPs was observed at 40.7°, which was situated between the peak positions of the (111) planes of Pd and Ir. This suggests the formation of a Pd-Ir alloy between the metallic phases. However, for the PdO-$IrO_2$ NPs calcinated in air, the diffraction peaks of Pd and Ir disappeared and new peaks appeared at different diffraction positions. These new peaks are consistent with the X-ray diffraction peaks of tetragonal-$IrO_2$ (JCPDS-88-0288) and tetragonal PdO (JCPDS-85-0713), suggesting that the Pd-Ir NPs were oxidized. This indicates that the alloying of the as-synthesized Pd-Ir NPs was incomplete. Subsequently, we calcinated the synthesized Pd-Ir NPs at 500°C in an Ar atmosphere to promote alloying (resulting in Pd-Ir alloy NPs).

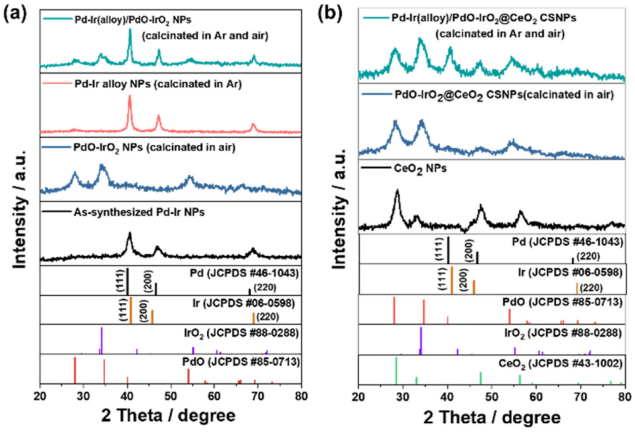


**Fig. 2.** XRD patterns of the as-synthesized (a) Pd-Ir NPs, (b) pure $CeO_2$ and Pd-Ir@$CeO_2$ CSNPs after the calcination process in Ar, air, and both Ar and air.

The results showed a decrease in the full width at half maximum (FWHM) and an increase in the peak intensity compared to those of the as-synthesized Pd-Ir NPs. To further confirm the alloying, the sample was further heat-treated at 500°C in an air atmosphere (resulting in Pd-Ir(alloy)/PdO-$IrO_2$ NPs). Compared to the PdO-$IrO_2$ NPs calcinated in air, the Pd-Ir(alloy)/PdO-$IrO_2$ NPs exhibited various X-ray diffraction peaks of Pd, Ir, PdO, and $IrO_2$. Furthermore, the peak of the (111) plane of the Pd-Ir alloy appeared at 40.7°, which matched that of the as-synthesized Pd-Ir NPs. Therefore, the results indicate that the calcination process in an Ar atmosphere facilitated the alloying of Pd-Ir NPs and consequently reduced oxidation. Fig. 2(b) shows the XRD profiles of the calcinated pure $CeO_2$ NPs and two other samples that heat-treated Pd-Ir@$CeO_2$ CSNPs at 500°C in different atmospheres: 1) in air atmosphere for 2 h, and 2) in Ar atmosphere for 2 h followed by an additional heat treatment in air. In these profiles, the X-ray diffraction peaks at 28.55°, 33.07°, 47.48°, 56.34°, 59.09°, 69.41°, 76.70°, and 79.07° correspond to the (111), (200), (220), (311), (222), (400), (331), and (420) planes of standard fcc-$CeO_2$ (JCPDS-43-1002) from. The $CeO_2$ NPs exhibited X-ray diffraction peaks consistent with fcc-$CeO_2$ crystals, while PdO-$IrO_2$@$CeO_2$ CSNPs calcinated in air atmosphere displayed X-ray diffraction peaks consistent with $IrO_2$, PdO, and $CeO_2$ crystals. Moreover, the Pd-Ir(alloy)/PdO-$IrO_2$@$CeO_2$ CSNPs calcinated in both Ar and air atmospheres exhibited X-ray diffraction peaks of Pd and Ir metals as well as metal oxides including PdO, $IrO_2$, and $CeO_2$. It indicates that alloying of the Pd-Ir core progressed through Ar calcination, resulting in relatively low oxidation by the alloying effect.

We conducted X-ray photoelectron spectroscopy (XPS) to investigate the electronic states of the surface elements. Fig. 3(a)

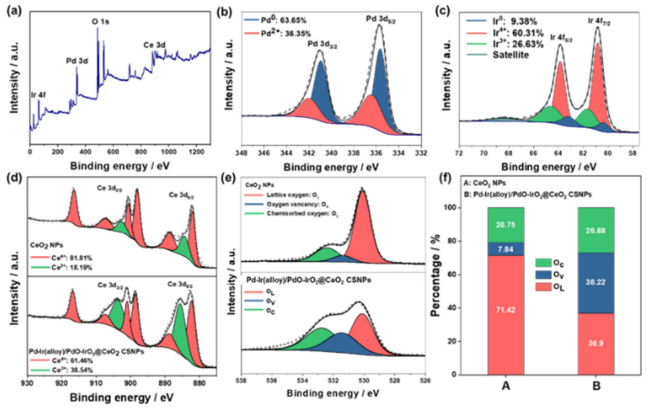

**Fig. 3.** High-resolution XPS spectra for (a) full range (b) Pd 3d, (c) Ir 4f in Pd-Ir(alloy)/PdO-$IrO_2$@$CeO_2$ CSNPs; (d) Ce 3d region and (e) O 1s region in the $CeO_2$ NPs and Pd-Ir(alloy)/PdO-$IrO_2$ @$CeO_2$ CSNPs; (f) the percentage of O 1s components in the $CeO_2$ NPs and Pd-Ir(alloy)/PdO-$IrO_2$ @$CeO_2$ CSNPs.

illustrates the comprehensive XPS spectrum of the Pd-Ir(alloy)/PdO-$IrO_2$@$CeO_2$ CSNPs including the Pd 3d, Ir 4f, Ce 3d, and O 1s spectra. In Fig. 3(b), the Pd 3d spectra of the Pd-Ir(alloy)/PdO-$IrO_2$@$CeO_2$ CSNPs containing the $3d_{5/2}$ and $3d_{3/2}$ components are fitted to four peaks. The peaks at 335.63 and 340.93 eV represent metallic Pd ($Pd^0$), while the peaks at 336.41 and 341.95 eV represent $Pd^{2+}$, reflecting Pd oxidation [44]. The percentage of $Pd^0$ was 63.65%, whereas that of $Pd^{2+}$ was 36.35%. Because Pd oxidation proceeds from the surface [28], these ratios indicate that oxidation is been significantly suppressed by alloying. Fig. 3(c) shows that the Ir 4f spectra of the Pd-Ir(alloy)/PdO-$IrO_2$@$CeO_2$ CSNPs containing the $4f_{7/2}$ and $4f_{5/2}$ components were segmented into six peaks. The peaks observed at 60.35 and 63.20 eV correspond to metallic Ir ($Ir^0$), while the peaks at 60.83 and 63.84 eV are attributed to $Ir^{4+}$, and the peaks at 61.64 and 64.60 eV correspond to $Ir^{3+}$ indicating the presence of $IrO_2$ [45]. The percentage ratios of $Ir^0$, $Ir^{3+}$, and $Ir^{4+}$ are 9.38, 26.63, and 60.31%, respectively. Considering that Ir is not extensively miscible with other metals, this indicates that Ir in the core is less alloyed than Pd [38]. Fig 3(d) shows the Ce 3d spectra of pure $CeO_2$ NPs and Pd-Ir(alloy)/PdO-$IrO_2$@$CeO_2$ CSNPs, containing $3d_{5/2}$ and $3d_{3/2}$ components. There are eight prominent peaks at energy levels of 882.5, 885.6, 889, 898.4, 901.1, 903.7, 917.6, and 916.8 eV, which are associated with Ce $3d_{3/2}$ and Ce $3d_{5/2}$ orbitals [46]. In addition, these peaks indicated the presence of both $Ce^{3+}$ and $Ce^{4+}$ oxidation states. The fraction of $Ce^{3+}$ in the $CeO_2$ NPs is 18.19%, while $Ce^{3+}$ in Pd-Ir(alloy)/PdO-$IrO_2$@$CeO_2$ CSNPs is 38.54%. The results showed that the core-shell structure had a higher $Ce^{3+}$ content owing to the interactions between $CeO_2$ and the Pd-Ir(alloy)/PdO-$IrO_2$ core. Typically, the production of $Ce^{3+}$ is accompanied by the formation of oxygen vacancies, indicating that the oxygen vacancy content of the Pd-Ir(alloy)/PdO-$IrO_2$@$CeO_2$ CSNPs is higher than that of pure $CeO_2$ NPs [47]. Fig. 3(e) illustrates the O 1s spectra of pure $CeO_2$ NPs and Pd-Ir(alloy)/PdO-$IrO_2$@$CeO_2$ CSNPs incorporating lattice oxygen ($O_L$), oxygen vacancies ($O_v$), and chemisorbed oxygen ($O_c$). The peaks observed at 529.8, 531.5, and 532.9 eV correspond to $O_L$, $O_v$, and $O_c$, respectively [48]. The sensing mechanism of the MOS gas sensor relies on the reaction between the adsorbed oxygen and the target gas, with the oxygen vacancies providing carriers. Therefore, it is crucial to confirm the contents of $O_v$ and $O_c$ [49-51]. The results indicated that the percentages of $O_c$ and $O_v$ were both significant in the Pd-Ir(alloy)/PdO-$IrO_2$@$CeO_2$ CSNPs compared to those in pure $CeO_2$ NPs as shown in Fig. 3(f). Furthermore, the increased amount of $O_v$ aligns with the high $Ce^{3+}$ content of the Pd-Ir(alloy)/PdO-$IrO_2$@$CeO_2$ CSNPs in the Ce 3d spectra.

### 3.2 Gas sensing performances

As MOS gas sensors operate thermally, it is essential to conduct sensing tests at various temperatures and gas concentrations to determine the optimal operating temperature. Fig. 4(a) shows the resistance change of the Pd-Ir(alloy)/PdO-$IrO_2$@$CeO_2$ CSNPs sensors to hydrogen gas at various operating temperatures (200-400°C) and concentrations (2-100 ppm). These results confirmed the $R_a$ and $R_g$ values, which were measured by evaluating the saturated sensor resistance in 10.5% oxygen after the injection of

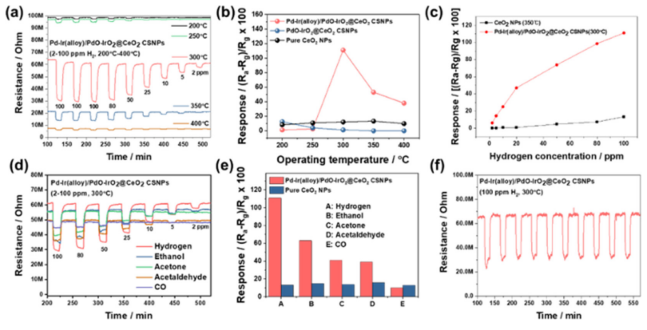

**Fig. 4.** Gas sensing properties of Pd-Ir(alloy)/PdO-$IrO_2$@$CeO_2$ CSNPs gas sensor with pure $CeO_2$ NPs or PdO-$IrO_2$@$CeO_2$ CSNPs sensors; (a) resistance changes for hydrogen gas; (b) response changes to 100 ppm $H_2$ at various operating temperatures with other sensors; (c) responses at various hydrogen concentrations at optimal working temperatures; (d) resistance changes at optimal working temperature depending upon gas concentration (2-100 ppm) of ethanol, acetone, acetaldehyde, and carbon monoxide; (e) hydrogen selectivity to different kinds of gasses at 100 ppm under the optimal working temperature; (f) ten cycle stability.

the test gas. Furthermore, the sensor response was calculated using the formula $R_s = (R_a - R_g) / R_g \times 100$ (%), as shown in Fig. 4(b). The results exhibit that the optimum operating temperatures for Pd-Ir(alloy)/PdO-$IrO_2$@$CeO_2$ CSNPs, PdO-$IrO_2$@$CeO_2$ CSNPs, and $CeO_2$ NPs gas sensors are 300°C, 200°C, and 350°C, respectively. In addition, the Pd-Ir(alloy)/PdO-$IrO_2$@$CeO_2$ CSNPs sensor showed the highest response value ($R_s$ = 111%) toward 100 ppm $H_2$ gas at the test temperature of 300°C, while the response of PdO-$IrO_2$@$CeO_2$ CSNPs sensor at 200°C was even lower than that of pure $CeO_2$ NPs sensor at 350°C. This indicates that preventing the oxidation of Pd-Ir NPs is crucial for the design of hydrogen gas sensing materials. Fig. 4(c) shows the sensitivities of the Pd-Ir(alloy)/PdO-$IrO_2$@$CeO_2$ CSNPs and pure $CeO_2$ NPs sensors under different hydrogen gas concentrations (2-100 ppm) at their optimum temperatures. The Pd-Ir(alloy)/PdO-$IrO_2$@$CeO_2$ CSNPs sensor displayed a linear response to hydrogen concentrations ranging from 2 to 100 ppm and exhibited improved sensitivity compared to the pristine $CeO_2$ sensor. For practical applications of gas sensors, high hydrogen selectivity toward target gases, as opposed to interfering gases, is crucial. To evaluate selectivity, the Pd-Ir(alloy)/PdO-$IrO_2$@$CeO_2$ CSNPs sensor was tested at 300°C with 100 ppm of hydrogen, ethanol, acetone, acetaldehyde, and carbon monoxide gases as shown in Figs. 4(d-e). The responses of the Pd-Ir(alloy)/PdO-$IrO_2$@$CeO_2$ CSNPs gas sensor to hydrogen, ethanol, acetone, methane, and carbon monoxide were 111, 63, 41, 39, and 10%, respectively. The responses of the pure $CeO_2$ NPs sensor to hydrogen, ethanol, acetone, methane, and carbon monoxide were 13.3, 14.9, 13.8, 15.9, and 12.7, respectively. These results indicate that the Pd-Ir(alloy)/PdO-$IrO_2$@$CeO_2$ CSNPs gas sensor exhibits higher hydrogen selectivity than the pure $CeO_2$ NPs sensor. To verify the stability of the Pd-Ir(alloy)/PdO-$IrO_2$@$CeO_2$ CSNPs gas sensor, ten cycles of 100 ppm $H_2$ gas injection were performed at the optimal operating temperature as shown in Fig. 4(f). Each cycle exhibited almost the same resistance change. This demonstrates that the resistance returned to the initial level when the hydrogen supply was stopped, confirming that the Pd-Ir(alloy)/PdO-$IrO_2$@$CeO_2$ CSNPs gas sensor has excellent repeatability.

### 3.3 Gas sensing mechanism

This section discusses the $H_2$ gas sensing mechanism of the Pd-Ir(alloy)/PdO-$IrO_2$@$CeO_2$ CSNPs sensor by comparing it with that of a pure $CeO_2$ NPs sensor, as shown in Fig. 5. The $H_2$ gas sensing mechanism is based on well-established principles for n-type semiconductor gas sensors [52-54]. When the sensor is

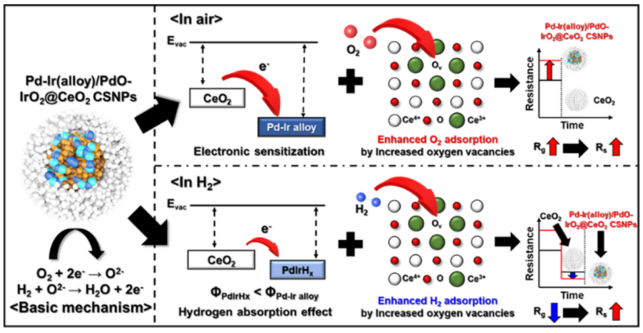


**Fig. 5.** Illustration for hydrogen gas sensing mechanism of Pd-Ir(alloy)/PdO-$IrO_2$@$CeO_2$ CSNPs, when exposed to air and hydrogen.

exposed to air, oxygen molecules are adsorbed on the surface of $CeO_2$ and capture electrons in the conduction band (CB), resulting in different oxygen species ($O^{2-}$, $O^-$, and $O^{2-}$) [55]. The type of ionized oxygen species depends on the operating temperature, as expressed by Eqs. (1-4). Since the optimal operating temperature of the sensing material was over 300°C, it is believed that $O^{2-}$ is the major adsorbed oxygen species.

$$O_2\ (gas) \rightarrow 2O\ (ads) \quad (1)$$
$$2O\ (ads) + e^- \rightarrow O_2^-\ (ads)\ (T < 100°C) \quad (2)$$
$$O\ (ads) + e^- \rightarrow O^-\ (ads)\ (100°C < T < 300°C) \quad (3)$$
$$O\ (ads) + 2e^- \rightarrow O^{2-}\ (ads)\ (T > 300°C) \quad (4)$$

These processes led to the formation of a depletion layer on the $CeO_2$ surface, ultimately increasing the baseline resistance ($R_a$). When $H_2$ gas was injected, the formed oxygen ions reacted with the $H_2$ molecules, releasing the captured electrons back into $CeO_2$. Consequently, the depletion layer becomes thinner, leading to a decrease in electrical resistance. The relevant reactions between the $H_2$ gas and oxygen ions are as follows:

$$H_2\ (gas) \rightarrow H_2\ (ads) \quad (5)$$
$$H_2\ (ads) + O^{2-} \rightarrow H_2O\ (ads) + 2e^- \quad (6)$$

In addition, the enhanced gas sensing performance of the Pd-Ir(alloy)/PdO-$IrO_2$@$CeO_2$ CSNPs sensor toward $H_2$ gas as compared to the pure $CeO_2$ NPs can be explained by two effects of the Pd-Ir alloy catalyst. The first is the catalytic effect [56-58] and the second is related to the hydrogen absorption effect (hydride formation) [59-61].

The catalytic effect includes both electronic and chemical sensitization effects. The electronic sensitization effect arises from the fact that the work function of $CeO_2$ (3.4 eV) is lower than those of Pd (5.2 eV) and Ir (5.1 eV) [46,62]. While combining these two processes, the electrons in the conduction band of $CeO_2$

are transferred to the surface of the Pd-Ir alloy NPs, resulting in the formation of a Schottky barrier at the interface. Consequently, the Pd-Ir(alloy)/PdO-$IrO_2$@$CeO_2$ CSNPs sensor exhibited a higher electrical resistance ($R_a$) in air. However, the chemical sensitization effect facilitates the easy dissociation of adsorbed hydrogen molecules into atoms by the Pd-Ir alloy nanoparticles, as shown in Eq. (7) [63-65]. The dissociated hydrogen atoms then migrate to the surface of $CeO_2$, where they react with active oxygen ions to form water, as shown in Eq. (8).

$$H_2\ (gas) \rightarrow 2H \quad (7)$$

$$2H + O^{2-} \rightarrow H_2O + 2e^- \quad (8)$$

As a result of this reaction, the fundamental gas-sensing mechanism is enhanced. Ultimately, this leads to a further decrease in electrical resistance in the presence of the target gases ($R_g$).

The second factor contributing to the enhanced hydrogen sensing performance of the Pd-Ir(alloy)/PdO-$IrO_2$@$CeO_2$ CSNPs sensor is the hydrogen absorption capability of the Pd-Ir alloy nanoparticles [35,66,67]. Duś et al. noted that the work function decreases when Pd absorbs hydrogen to form Pd hydride [24]. This change in the work function is influenced by the redistribution of the electric charge resulting from chemical reactions on the surface. A decrease in the work function has been observed for several transition-metal hydrides, which is attributed to the presence of highly polarized hydrogen species on the surface. Therefore, when the Pd-Ir alloy nanoparticles absorb hydrogen and are partially converted to Pd-Ir hydride on their surfaces, as described in Eq. (9), the work function of the Pd-Ir alloy nanoparticles is reduced.

$$PdIr + xH \rightarrow PdIrH_x \quad (9)$$

Consequently, the height of the Schottky barrier between the Pd and Ir alloy and $CeO_2$ was reduced, leading to a decrease in the electric depletion layer. This effect lowers the electrical resistance in the presence of hydrogen gas. The reaction described in Eq. (9) occurs selectively for hydrogen gas, which further explains the high selectivity of the Pd-Ir(alloy)/PdO-$IrO_2$@$CeO_2$ CSNPs sensor toward $H_2$.

In addition, as described above, the Pd-Ir(alloy)/PdO-$IrO_2$@$CeO_2$ CSNPs with a core-shell structure showed significantly higher amounts of $Ce^{3+}$ and oxygen vacancies than pure $CeO_2$ NPs. The presence of these oxygen vacancies plays a crucial role in gas-sensing performance because they are capable of generating electrons. Moreover, these vacancies served as active sites for the adsorption of both oxygen and hydrogen gases. Therefore, the increased number of oxygen vacancies helps create an environment that facilitates interactions between oxygen and hydrogen gas, such as adsorption onto the $CeO_2$ surface. Hence, this demonstrates the importance of structural modifications in enhancing gas-sensing performance.

## 4. CONCLUSIONS

Pd-Ir composite NPs with an average diameter of 19 nm were successfully synthesized by a hydrothermal method and used as seeds to obtain Pd-Ir@$CeO_2$ CSNPs with particle sizes in the range of 36-42 nm. For alloying the Pd-Ir core, heat treatments were performed sequentially at 500°C in an Ar atmosphere for 2 h and in an air atmosphere for 2 h, and as a result, Pd-Ir(alloy)/PdO-$IrO_2$@$CeO_2$ CSNPs with a hollow alloy core were obtained.

The Pd-Ir(alloy)/PdO-$IrO_2$@$CeO_2$ CSNP sensor showed a response of 111% to 100 ppm $H_2$ gas, which was significantly higher than those of fully oxidized PdO-$IrO_2$@$CeO_2$ CSNPs and pure $CeO_2$ NP sensors. The selectivity for hydrogen gas was significantly higher than that for ethanol, acetone, acetaldehyde, and CO. The enhanced hydrogen gas sensing properties of the Pd-Ir(alloy)/PdO-$IrO_2$@$CeO_2$ CSNPs sensor are attributed to the hydrogen absorption and catalytic effects of the Pd-Ir(alloy) core on the hydrogen oxidation reaction. In addition, $PdIrH_x$ formed by hydrogen adsorption lowers the Schottky barrier between PdIr and $CeO_2$, resulting in a decrease in the resistance of the sensor and an increase in sensitivity.

## ACKNOWLEDGMENT

This work was supported by 1) BK21-FOUR programs of the Ministry of Education and Human-Resource Development, South Korea; 2) National Research Foundation of Korea (NRF) grant funded by the Korean government (MSIP) (2021R1A2C2008447); 3) "Regional Innovation Strategy (RIS)" through the National Research Foundation of Korea(NRF) funded by the Ministry of Education (MOE) (2023RIS-008).

## REFERENCES

[1] S. Okazaki, H. Kawada, Y. Koshiba, N. Kasai, Y. Maru, T. Mizutani, Y. Takesaki, and S. Shimano, “Catalytic combustion type optical fiber Bragg grating hydrogen gas sensor using platinum-loaded fumed silica powder”, *Int. J.*

*Hydrogen Energy*, Vol. 48, No. 25, pp. 9512-9527, 2023.
[2] C.-M. Wu, K. G. Motora, G.-Y. Chen, D.-H. Kuo, and N. S. Gultom, "Highly efficient reduced tungsten oxide-based hydrogen gas sensor at room temperature", *Mater. Sci. Eng. B*, Vol. 289, p. 116285, 2023.
[3] W. Son, D. W. Lee, Y. K. Kim, S. Chun, J. M. Lee, J. H. Choi, W. S. Shim, D. Suh, S. K. Lim, and C. Choi, "PdO-nanoparticle-embedded carbon nanotube yarns for wearable hydrogen gas sensing platforms with fast and sensitive responses", *ACS Sens.*, Vol. 8, No. 1, pp. 94-102, 2023.
[4] H. Cai, N. Luo, X. Wang, M. Guo, X. Li, B. Lu, Z. Xue, and J. Xu, "Kinetics?Driven Dual Hydrogen Spillover Effects for Ultrasensitive Hydrogen Sensing", *Small*, Vol. 19, No. 42, p. 2302652, 2023.
[5] X. Wang, X. Meng, Y. Zhu, and W. Gao, "Design of ultra-high-response gas sensor based on Pd-$WO_3$/$WS_2$ ternary nanocomposites for ultrafast hydrogen detection", *Sens. Actuators B Chem.*, Vol. 401, p. 134991, 2024.
[6] V. N. Rao, P. K. Sairam, M. D. Kim, M. Rezakazemi, T. M. Aminabhavi, C. W. Ahn, and J. M. Yang, "CdS/$TiO_2$ nano hybrid heterostructured materials for superior hydrogen production and gas sensor applications", *J. Environ. Manage.*, Vol. 340, p. 117895, 2023.
[7] A. Umar, S. Akbar, R. Kumar, J. N. O. Amu-Darko, S. Hussain, A. A. Ibrahim, M. A. Alhamami, N. Almehbad, T. Almas, and A. F. Seliem, "Ce-doped ZnO nanostructures: A promising platform for $NO_2$ gas sensing", *Chemosphere*, Vol. 349, p. 140838, 2024.
[8] X. Wang, Y. Li, X. Jin, G. Sun, J. Cao, and Y. Wang, "The effects of Co doping on the gas sensing performance of $In_2O_3$ porous nanospheres", *Sens. Actuators B Chem.*, Vol. 403, p. 135155, 2024.
[9] J. Zhao, H. Wang, Y. Cai, J. Zhao, Z. Gao, and Y.-Y. Song, "The challenges and opportunities for $TiO_2$ nanostructures in gas sensing", *ACS Sens.*, Vol. 9, No. 4, pp. 1644-1655, 2024.
[10] K. H. Prasad, S. Vinoth, S. Valanarasu, B. Prakash, Z. Ahmad, T. Alshahrani, and M. Shkir, "Exploring the ammonia gas sensing properties of Gd doped $CeO_2$ thin films deposited by spray pyrolysis method", *J. Alloys Compd.*, Vol. 1002, p. 175415, 2024.
[11] J. Y. Kim, B. Jang, M. Lim, J. Y. Park, and Y.-H. Choa, "Enhanced PtRu by $CeO_2$ hollow nanofibers: Hydrogen gas sensing with CO-resistant in fuel cell", *J. Power Sources*, Vol. 613, p. 234842, 2024.
[12] T. M. Nimbalkar, S. A. Kadam, Y. R. Ma, A. C. Khot, M. Selvaraj, Z. Ahmad, and V. B. Patil, "Zn mixed $CeO_2$ nanoparticles: Enhancement of $NO_2$ gas sensing performance", *J. Alloys Compd.*, Vol. 987, p. 174109, 2024.
[13] S. Hussain, N. Aslam, X. Y. Yang, M. S. Javed, Z. Xu, M. Wang, G. Liu, and G. Qiao, "Unique polyhedron $CeO_2$ nanostructures for superior formaldehyde gas-sensing performances", *Ceram. Int.*, Vol. 44, No. 16, pp. 19624-19630, 2018.
[14] D. Van Dao, T. T. D. Nguyen, S. M. Majhi, G. Adilbish, H. J. Lee, Y. T. Yu, and I. H. Lee, "Ionic liquid-supported synthesis of $CeO_2$ nanoparticles and its enhanced ethanol gas sensing properties", *Mater. Chem. Phys.*, Vol. 231, pp. 1-8, 2019.
[15] V. T. Duoc, H. Nguyen, T. M. Ngoc, C. T. Xuan, C. M. Hung, N. Van Duy, and N. D. Hoa, "Hydrogen gas sensor based on self-heating effect of $SnO_2$/Pt thin film with ultralow power consumption", *Int. J. Hydrogen Energy*, Vol. 61, pp. 774-782, 2024.
[16] Y. Nagarjuna and Y.-J. Hsiao, "$TeO_2$ doped ZnO nanostructure for the enhanced $NO_2$ gas sensing on MEMS sensor device", *Sens. Actuators B Chem.*, Vol. 401, p. 134891, 2024.
[17] V. K. Premkumar, R. Vishnuraj, T. S. Sheena, X. Yang, B. Pullithadathil, C. Zhang, and Z. Wu, "Influence of ZnO hexagonal pyramid nanostructures for highly sensitive and selective $NO_2$ gas sensor", *J. Alloys Compd.*, Vol. 994, p. 174625, 2024.
[18] C. Sun, J. Shao, G. Pan, and X. Yang, "Triethylamine gas sensor based on $Zn_2SnO_4$ polyhedron decorated with Au nanoparticles and density functional theory investigation", *Sens. Actuators B Chem.*, Vol. 408, p. 135510, 2024.
[19] D. Kong, B. Ma, L. Zhang, L. Yang, C. Li, C. Yin, K. Wu, and Y. Wang, "Metal (Au, Ag, Pt) Doping Effects on the Gas-Sensing Mechanism and Characteristics of Two-Dimensional $WS_2$: A First-Principle", *ACS Appl. Electron. Mater.*, Vol. 6, No. 2, pp. 958-968, 2024.
[20] T. Zeng, D. Ma, and Y. Gui, "Gas-Sensitive Performance Study of Metal (Au, Pd, Pt)/ZnO Heterojunction Gas Sensors for Dissolved Gases in Transformer Oil", *Langmuir*, Vol. 40, No. 18, pp. 9819-9830, 2024.
[21] A. Mirzaei, H. R, Yousefi, F. Falsafi, M. Bonyani, J. H. Lee, J. H. Kim, H. W. Kim, and S. S. Kim, "An overview on how Pd on resistive-based nanomaterial gas sensors can enhance response toward hydrogen gas", *Int. J. Hydrogen Energy*, Vol. 44, No. 36, pp. 20552-20571, 2019.
[22] L. Moumaneix, A. Rautakorpi, and T. Kallio, "Interactions between hydrogen and palladium nanoparticles: resolving adsorption and absorption contributions", *ChemElectroChem*, Vol. 10, No. 6, p. e202201109, 2023.
[23] J. Y. Kim, K. Choi, S. W. Kim, C. W. Park, S. I. Kim, A. Mirzaei, J. H. Lee, and D. Y. Jeong, "Enhancement of $H_2$ Gas Sensing Using Pd Decoration on ZnO Nanoparticles", *Chemosensors*, Vol. 12, No. 6, p. 90, 2024.
[24] R. Duś, R. Nowakowski, and E. Nowicka, "Chemical and structural components of work function changes in the process of palladium hydride formation within thin Pd film", *J. Alloys Compd.*, Vol. 404, pp. 284-287, 2005.
[25] Z. Cai, J. Park, and S. Park, "Synergistic effect of Pd and $Fe_2O_3$ nanoparticles embedded in porous NiO nanofibers on hydrogen gas detection: Fabrication, characterization, and sensing mechanism exploration", *Sens. Actuators B Chem.*, Vol. 388, p. 133836, 2023.
[26] X. Meng, M. Bi, Q. Xiao, and W. Gao, "Ultra-fast response and highly selectivity hydrogen gas sensor based on Pd/$SnO_2$ nanoparticles", *Int. J. Hydrogen Energy*, Vol. 47, No. 5, pp. 3157-3169, 2022.
[27] T. Thathsara, C. J. Harrison, D. Schönauer-Kamin, U. Mansfeld, R. Moos, F. M. Malherbe, R. K. Hocking, and M. Shafiei, "Pd Nanoparticles Decorated Hollow $TiO_2$ Nanospheres for Highly Sensitive and Selective UV-Assisted

Hydrogen Gas Sensors", *ACS Appl. Energy Mater.*, Vol. 7, No. 14, pp. 5608-5620, 2024.

[28] D. Zhang, C. Jin, H. Tian, Y. Xiong, H. Zhang, P. Qiao, J. Fan, Z. Zhang, Z. Y. Li, and J. Li, "An In situ TEM study of the surface oxidation of palladium nanocrystals assisted by electron irradiation", *Nanoscale*, Vol. 9, No. 19, pp. 6327-6333, 2017.

[29] S. Kumar, S. D. Lawaniya, S. R. Nelamarri, M. Kumar, P. K. Dwivedi, Y. T. Yu, Y. K. Mishra, and K. Awasthi, "Bimetallic Ag-Pd nanoparticles decorated ZnO nanorods for efficient hydrogen sensing", *Sens. Actuators B Chem.*, Vol. 394, p. 134394, 2023.

[30] X. Meng, M. Bi, and W. Gao, "PdAg alloy modified $SnO_2$ nanoparticles for ultrafast detection of hydrogen", *Sens. Actuators B Chem.*, Vol. 382, p. 133515, 2023.

[31] S. B. Eadi, J. S. Oh, C. Kim, G. Sim, K. Kim, H. Y. Kim, J. J. Kim, H. R. Do, S.-I. Chu, S. H. Jung, and H. D. Lee, "Improved hydrogen gas sensing performance of Pd–Ni alloy thin films", *Int. J. Hydrogen Energy*, Vol. 48, No. 33, pp. 12534-12539, 2023.

[32] G. Pandey, M. Bhardwaj, S. Kumar, S. D. Lawaniya, M. Kumar, P. K. Dwivedi, and K. Awasthi, "Synergistic effects of Pd-Ag decoration on $SnO/SnO_2$ nanosheets for enhanced hydrogen sensing", *Sens. Actuators B Chem.*, Vol. 402, p. 135062, 2024.

[33] P. G. Choi and Y. Masuda, "Surface modification of nanosheet-type tin oxide with Au-Pd for hydrogen gas sensing", *J. Alloys Compd.*, Vol. 960, p. 170888, 2023.

[34] J. Li, Z. Yuan, Z. Mu, Z. Yang, and F. Meng, "Synergistic catalytic effect of PdPt bimetallic alloy for room temperature hydrogen detection", *Sens. Actuators B Chem.*, Vol. 405, p. 135404, 2024.

[35] H. Kobayashi, M. Yamauchi, R. Ikeda, T. Yamamoto, S. Matsumura, and H. Kitagawa, "Double enhancement of hydrogen storage capacity of Pd nanoparticles by 20 at% replacement with Ir; systematic control of hydrogen storage in Pd–M nanoparticles (M= Ir, Pt, Au)", *Chem. Sci.*, Vol. 9, No. 25, pp. 5536-5540, 2018.

[36] T. Yayama, T. Ishimoto, and M. Koyama, "Effect of alloying elements on hydrogen absorption properties of palladium-based solid solution alloys", *J. Alloys Compd.*, Vol. 653, pp. 444-452, 2015.

[37] M. LaPrade, K. D. Allard, J. F. Lynch, and T. B. Flanagan, "Absorption of hydrogen by iridium/palladium substitutional alloys", *J. Chem. Soc. Faraday Trans. 1*, Vol. 70, pp. 1615-1630, 1974.

[38] H. Guo, H. Li, K. Jarvis, H. Wan, P. Kunal, S. G. Dunning, Y. Liu, G. Henkelman, and S. M. Humphrey, "Microwave-assisted synthesis of classically immiscible Ag–Ir alloy nanoparticle catalysts", *ACS Catal.*, Vol. 8, No. 12, pp. 11386-11397, 2018.

[39] M. Zahmakiran, "Iridium nanoparticles stabilized by metal organic frameworks (IrNPs@ ZIF-8): synthesis, structural properties and catalytic performance", *Dalton Trans.*, Vol. 41, No. 41, pp. 12690-12696, 2012.

[40] W. Liu, Y. Magnin, D. Förster, J. Bourgon, T. Len, F. Morfin, L. Piccolo, H. Amara, and C. Zlotea, "Size-dependent hydrogen trapping in palladium nanoparticles", *J. Mater Chem. A*, Vol. 9, No. 16, pp. 10354-10363, 2021.

[41] M. Yamauchi, R. Ikeda, H. Kitagawa, and M. Takata, "Nanosize effects on hydrogen storage in palladium", *The J. Phys. Chem. C*, Vol. 112, No. 9, pp. 3294-3299, 2008.

[42] H. Guo, Z. Fang, H. Li, D. Fernandez, G. Henkelman, S. M. Humphrey, and G. Yu, "Rational design of rhodium–iridium alloy nanoparticles as highly active catalysts for acidic oxygen evolution", *ACS Nano*, Vol. 13, No. 11, pp. 13225-13234, 2019.

[43] Y. Yin, R. M. Rioux, C. K. Erdonmez, S. Hughes, G. A. Somorjai, and A. P. Alivisatos, "Formation of hollow nanocrystals through the nanoscale Kirkendall effect," *Sci.*, Vol. 304, No. 5671, pp. 711-714, 2004.

[44] X. Wang, J. Chen, J. Zeng, Q. Wang, Z. Li, R. Qin, C. Wu, Z. Xie, and L. Zheng, "The synergy between atomically dispersed Pd and cerium oxide for enhanced catalytic properties", *Nanoscale*, Vol. 9, No. 20, pp. 6643-6648, 2017.

[45] Z. S. H. S. Rajan, T. Binninger, P. J. Kooyman, D. Susac, and R. Mohamed, "Organometallic chemical deposition of crystalline iridium oxide nanoparticles on antimony-doped tin oxide support with high-performance for the oxygen evolution reaction", *Catal. Sci. Technol.*, Vol. 10, No. 12, pp. 3938-3948, 2020.

[46] J. M. Ferreira Jr, K. P. Souza, F. M. Queiroz, I. Costa, and C. R. Tomachuk, "Electrochemical and chemical characterization of electrodeposited zinc surface exposed to new surface treatments", *Surf. Coat. Technol.*, Vol. 294, pp. 36-46, 2016.

[47] Q. Hu, H. Jiang, W. Zhang, X. Wang, X. Wang, and Z. Zhang, "Unveiling the synergistic effects of hydrogen annealing on $CeO_2$ nanofibers for highly sensitive acetone gas detection: Role of $Ce^{3+}$ ions and oxygen vacancies", *Appl. Surf. Sci.*, Vol. 640, p. 158411, 2023.

[48] J. Lian, P. Liu, C. Jin, Z. Shi, X. Luo, and Q. Liu, "Perylene diimide-functionalized $CeO_2$ nanocomposite as a peroxidase mimic for colorimetric determination of hydrogen peroxide and glutathione", *Microchim. Acta*, Vol. 186, pp. 1-9, 2019.

[49] G. Jung, S. Ju, K. Choi, J. Kim, S. Hong, J. Park, W. Shin, Y. Jeong, S. Han, W. Y. Choi, and J. H. Lee, "Reconfigurable manipulation of oxygen content on metal oxide surfaces and applications to gas sensing", *ACS Nano*, Vol. 17, No. 18, pp. 17790-17798, 2023.

[50] L. Liu, Y. Wang, K. Guan, Y. Liu, Y. Li, F. Sun, X. Wang, C. Zhang, S. Feng, and T. Zhang, "Influence of oxygen vacancies on the performance of $SnO_2$ gas sensing by near-ambient pressure XPS studies", *Sens. Actuators B Chem.*, Vol. 393, p. 134252, 2023.

[51] K. Sun, G. Zhan, L. Zhang, Z. Wang, and S. Lin, "Highly sensitive $NO_2$ gas sensor based on ZnO nanoarray modulated by oxygen vacancy with Ce doping", *Sens. Actuators B Chem.*, Vol. 379, p. 133294, 2023.

[52] N. Barsan and U. Weimar, "Conduction model of metal oxide gas sensors", *J. Electroceram.*, Vol. 7, pp. 143-167, 2001.

[53] N. Goel, K. Kunal, A. Kushwaha, and M. Kumar, "Metal oxide semiconductors for gas sensing", *Eng. Rep.*, Vol. 5, No. 6, p. e12604, 2023.

[54] N. Yamazoe, G. Sakai, and K. Shimanoe, "Oxide semiconductor gas sensors", *Catal. Surv. Asia*, Vol. 7, pp. 63-75, 2003.

[55] J. Sun, G. Yin, T. Cai, W. Yu, F. Peng, Y. Sun, F. Zhang, J. Lu, M. Ge, and D. He, "The role of oxygen vacancies in the sensing properties of Ni substituted $SnO_2$ microspheres", *RSC Adv.*, Vol. 8, No. 58, pp. 33080-33086, 2018.

[56] D. J. Yu, W. Oum, A. Mirzaei, K. Y. Shin, E. B. Kim, H. M. Kim, S. S. Kim, and H. W. Kim, "Enhancement of xylene gas sensing by using Au core structures in regard to Au@$SnO_2$ core-shell nanocomposites", *Sens. Actuators B Chem.*, Vol. 392, p. 134018, 2023.

[57] H. Cui, M. Ran, X. Peng, and G. Zhang, "First-principles design of noble metal (Rh and Pd) dispersed Janus WSTe monolayer for toxic gas sensing applications", *J. Environ. Chem. Eng.*, Vol. 12, No. 2, p. 112047, 2024.

[58] J. Zhang, W. Feng, Y. Zhang, W. Zeng, and Q. Zhou, "Gas-sensing properties and first-principles comparative study of metal (Pd, Pt)-decorated $MoSe_2$ hierarchical nanoflowers for efficient $SO_2$ detection at room temperature", *J. Alloys Compd.*, Vol. 968, p. 172006, 2023.

[59] Z. Li, X. Xing, D. Feng, L. Du, Y. Tian, X. Chen, and D. Yang, "Nitrogen-doped carbon microfibers decorated with palladium and palladium oxide nanoparticles for high-concentration hydrogen sensing", *Ceram. Int.*, Vol. 50, No. 12, pp. 21519-21525, 2024.

[60] Q. Li, L. Wang, A. Xiao, L. Zhu, and Z. Yang, "Hydrogen sensing towards palladium-based nanocomposites: A review", *Int. J. Hydrogen Energy*, https://www.sciencedirect.com/science/article/abs/pii/S036031992400003X, 2024.

[61] Z. Chen, P. Yuan, C. Chen, X. Wang, J. Wang, J. Jia, B. Davaasuren, Z. Lai, N. M. Khashab, K.-W. Huang, O. M. Bakr, J. Yin, and K. N. Salama, "Balancing Pd–H Interactions: Thiolate?Protected Palladium Nanoclusters for Robust and Rapid Hydrogen Gas Sensing", *Adv. Mater.*, https://doi.org/10.1002/adma.202404291, p. 2404291, 2024.

[62] T. T. Nguyet, D. T. T. Le, N. Van Duy, C. T. Xuan, S. Ingebrandt, X. T. Vu, and N. D. Hoa, "A sigh-performance hydrogen gas sensor based on Ag/Pd nanoparticle-functionalized ZnO nanoplates", *RSC Adv.*, Vol. 13, No. 19, pp. 13017-13029, 2023.

[63] N. Luo, Y. Chen, D. Zhang, M. Guo, Z. Xue, X. Wang, Z. Cheng, and J. Xu, "High-sensitive MEMS hydrogen sulfide sensor made from PdRh bimetal hollow nanoframe decorated metal oxides and sensitization mechanism study", *ACS Appl. Mater. Interfaces*, Vol. 12, No. 50, pp. 56203-56215, 2020.

[64] X. Yang, Y. Deng, H. Yang, Y. Liao, X. Cheng, Y. Zou, L. Wu, and Y. Deng, "Functionalization of mesoporous semiconductor metal oxides for gas sensing: Recent advances and emerging challenges", *Adv. Sci.*, Vol. 10, No. 1, p. 2204810, 2023.

[65] S. Agarwal, S. Kumar, H. Agrawal, M. G. Moinuddin, M. Kumar, S. K. Sharma, and K. Awasthi, "An efficient hydrogen gas sensor based on hierarchical Ag/ZnO hollow microstructures", *Sens. Actuators B Chem.*, Vol. 346, p. 130510, 2021.

[66] P. Das, Y.-S. Lee, S.-C. Lee, and S. Bhattacharjee, "Computational design of a new palladium alloy with efficient hydrogen storage capacity and hydrogenation-dehydrogenation kinetics", *Int. J. Hydrogen Energy*, Vol. 48, No. 49, pp. 18795-18803, 2023.

[67] K. Hubkowska, M. Pająk, and A. Czerwiński, "Hydrogen electrosorption properties of electrodeposited Pd-Ir alloys", *J. Solid State Electrochem.*, Vol. 26, No. 1, pp. 103-109, 2022.